Original article

# Dual mass spectrometry imaging and spatial metabolomics to investigate the metabolism and nephrotoxicity of nitidine chloride

Shu Yang [a], Zhonghua Wang [b, c, d, **], Yanhua Liu [c], Xin Zhang [c], Hang Zhang [a], Zhaoying Wang [b, c], Zhi Zhou [b, c], Zeper Abliz [a, b, c, d, *]

[a] School of Pharmacy, Minzu University of China, Beijing, 100081, China
[b] Key Laboratory of Mass Spectrometry Imaging and Metabolomics (Minzu University of China), National Ethnic Affairs Commission, Beijing, 100081, China
[c] Center for Imaging and Systems Biology, College of Life and Environmental Sciences, Minzu University of China, Beijing, 100081, China
[d] Key Laboratory of Ethnomedicine of Ministry of Education, School of Pharmacy, Minzu University of China, Beijing, 100081, China

## ARTICLE INFO

## ABSTRACT

Evaluating toxicity and decoding the underlying mechanisms of active compounds are crucial for drug development. In this study, we present an innovative, integrated approach that combines air flow-assisted desorption electrospray ionization mass spectrometry imaging (AFADESI-MSI), time-of-flight secondary ion mass spectrometry (ToF-SIMS), and spatial metabolomics to comprehensively investigate the nephrotoxicity and underlying mechanisms of nitidine chloride (NC), a promising anti-tumor drug candidate. Our quantitive AFADESI-MSI analysis unveiled the region specific of accumulation of NC in the kidney, particularly within the inner cortex (IC) region, following single and repeated dose of NC. High spatial resolution ToF-SIMS analysis further allowed us to precisely map the localization of NC within the renal tubule. Employing spatial metabolomics based on AFADESI-MSI, we identified over 70 discriminating endogenous metabolites associated with chronic NC exposure. These findings suggest the renal tubule as the primary target of NC toxicity and implicate renal transporters (organic cation transporters, multidrug and toxin extrusion, and organic cation transporter 2 (OCT2)), metabolic enzymes (protein arginine N-methyltransferase (PRMT) and nitric oxide synthase), mitochondria, oxidative stress, and inflammation in NC-induced nephrotoxicity. This study offers novel insights into NC-induced renal damage, representing a crucial step towards devising strategies to mitigate renal damage caused by this compound.

## 1. Introduction

*Zanthoxylum nitidum* (Roxb.) DC, also known as Liang-Mian-Zhen in China, has been used for centuries in traditional Chinese medicine to treat various ailments, including stomach aches, toothaches, rheumatic pain, injuries, and venomous snake bites [1]. Nitidine chloride (NC) is an active quaternary ammonium alkaloid that is mainly extracted from the root of *Zanthoxylum nitidum* (Roxb.) DC [2]. Several studies have demonstrated the diverse biological activities of NC, including anti-inflammatory, antimalarial, antifungal, and antiviral properties [3–6]. Moreover, NC has

been a promising anti-tumor drug candidate due to its ability to inhibit the proliferation of various cancer types, such as hepatocellular carcinoma and gastric cancer, as well as impede the metastasis of breast cancer, ovarian cancer, and osteosarcoma [7–11]. However, some concerns have arisen regarding its toxicity, particularly its potential hepatotoxicity, cardiotoxicity, and nephrotoxicity, despite its promising biological activities [12–14]. Thus, further studies are urgently required to determine its nephrotoxicity, understand the underlying toxic mechanisms, and promote its development as an anti-tumor drug.

The kidney is a crucial organ responsible for maintaining the body's homeostasis and metabolism by regulating acid-base balance, eliminating harmful chemical waste, and excreting metabolites. It is one of the major target organs in drug or chemical-induced toxicity. *In vitro* studies have indicated the crucial roles of organic cation transporter 2 (OCT2) and multidrug and toxin extrusion 1 (MATE1) in NC-induced nephrotoxicity [14]. However, the kidney is highly heterogeneous and is composed of various cell types with
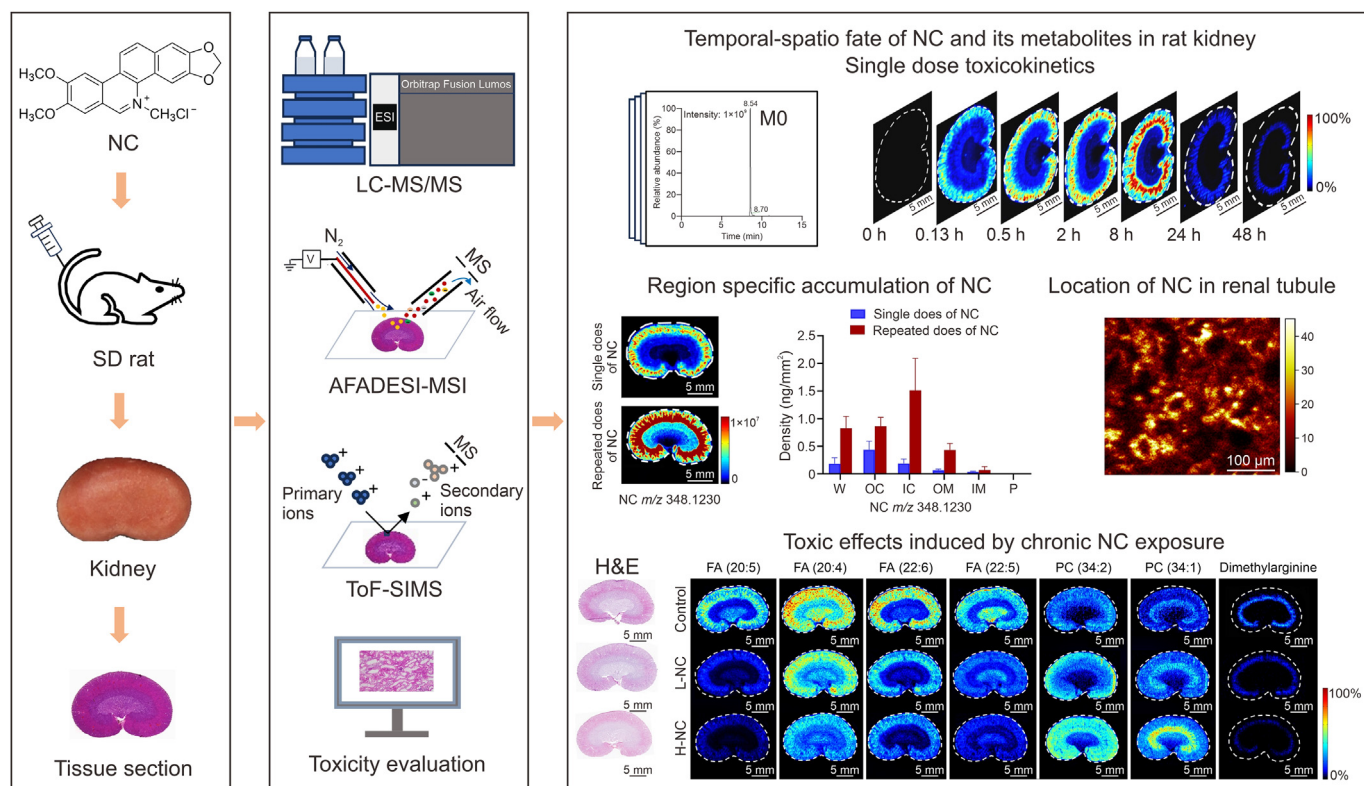
Fig. 1. Research strategy for spatially-resolved metabolomics in nephrotoxicity of nitidine chloride (NC). SD: Sprague-Dawley; ESI: electrospray ionization; LC-MS/MS: liquid chromatography with tandem mass spectrometry; AFADESI-MSI: the air flow-assisted desorption electrospray ionization mass spectrometry imaging; ToF-SIMS: time-of-flight secondary ion mass spectrometry; M0: NC; W: whole renal section; OC: outer cortex; IC: inner cortex; OM: outer medulla; IM: inner medulla; P: papilla; H&E: hematoxylin and eosin; L-NC: low-dose NC (2 mg/kg) group; H-NC: high-dose NC (6 mg/kg) group; FA: fatty acid; PC: phosphatidylcholine.

distinct functions and molecular profiles. This heterogeneity poses a significant challenge in understanding the mechanisms underlying NC-induced nephrotoxicity, because the toxic effects may vary depending on the target cells and tissues. Therefore, investigating the regional toxicokinetics and toxicodynamics of NC within the kidney may provide valuable insights into the molecular and cellular changes associated with NC-induced toxicity.

Mass spectrometry imaging (MSI) is a powerful and label-free molecular imaging tool that allows visualization and quantification of multiple known or unknown molecules in tissues and organs [15,16]. It is particularly useful in investigating drug toxicokinetics because it enables mapping the distribution and localization of parent compounds and their metabolites in tissues [17,18]. This approach helps identify target tissues and visualize drug accumulation in specific organ/body regions. Compared to targeted toxicological methods, such as immunohistochemistry (IHC) [19], MSI does not focus on any specific analyte. Instead, it provides a high-throughput and unbiased evaluation of the local biochemical responses of tissues to toxic stimuli. Therefore, MSI can identify novel in situ toxic biomarkers and targets, making it a promising tool for toxicodynamics studies. Desorption electrospray ionization (DESI)-MSI, time-of-flight secondary ion mass spectrometry (ToF-SIMS), and matrix-assisted laser desorption ionization (MALDI)-MSI are the three primary MSI modalities, each with distinct advantages and drawbacks for metabolite imaging. For instance, ToF-SIMS excels in high-resolution metabolite imaging with detailed spatial analysis using high-energy primary ions but faces challenges with fragment ions and limited applicability to certain biomolecules [20]. DESI-MSI offers versatility and softer ionization, making it suitable for various small molecules [21].

Ambient air-flow-assisted desorption electrospray ionization (AFADESI)-MSI provides high sensitivity and broad coverage for untargeted analysis, allowing simultaneous visualization of thousands of metabolites [22]. However, DESI-MSI and AFADESI-MSI have a spatial resolution of approximately 100 μm, restricting their use in high spatial resolution MSI analyses [23].

While studies on toxicokinetics and toxicodynamics using MSI and MSI-based spatial metabolomics have yielded promising results, they are still in their early stages. Lin et al. [24] utilized high spatial resolution ToF-SIMS imaging visualization of cisplatin imaging in single cells, and revealed cisplatin regulating interactions between transcription factors and DNA. Our group proposed a highly specific and sensitive in situ metabolomics method based AFADESI-MSI, revealing spatially resolved metabolic changes in the kidney of rats after aristolochic acid administration [25]. In addition, Stoffels et al. [26] employed MALDI-MSI and ToF-SIMS techniques to illustrate the heterogeneous distribution of perfluorooctanoic acid, highlighting its localized impact on lipid expression.

In this study, we present an innovative integrated approach that harmonizes AFADESI-MSI, ToF-SIMS, and spatially-resolved metabolomics for a comprehensive exploration of the regional toxicokinetics and toxicodynamics of NC in rat kidneys. Initially, multiple first-phase and second-phase metabolites of NC in rat kidneys after a single dose of NC were identified using high-resolution liquid chromatography with tandem mass spectrometry (LC-MS/MS). Subsequently, we employed an AFADESI system coupled with an ultra-high-resolution quadrupole-Orbitrap-quadrupole ion-trap (Q-OT-qIT) MS to quantitively visualize the temporospatial distribution of NC and its metabolites after single and repeated dose of NC. In addition, we accurately mapped the precise

localization of NC within the kidney using high spatial resolution ToF-SIMS. Finally, the region-specific spatial alteration of endogenous metabolites that cross the rat kidneys after repeated doses of NC for 21 days was discovered by spatial metabolomics based on AFADESI-MSI. The research strategy is depicted in Fig. 1, providing an overview of our comprehensive approach.

## 2. Materials and methods

### 2.1. Chemicals and reagents

NC was purchased from Chengdu Desite Biological Technology Co., Ltd. (Chengdu, China). High-performance liquid chromatography (HPLC)-grade methanol (MeOH), acetonitrile (ACN), isopropanol (IPA), and formic acid were obtained from Fisher Scientific (Loughborough, UK). Ultrapure water was obtained from Wahaha Co., Ltd. (Hangzhou, China). Hydroxypropyl-β-cyclodextrin was purchased from J&K Scientific (Beijing, China). Silicon wafers was purchased from Jingmei Hongye Technology Co., Ltd. (Beijing, China).

### 2.2. Animal experiments

We purchased Sprague-Dawley rats (male, 180−200 g) from Vital River Laboratory Animal Technology Co., Ltd. (Beijing, China). The animals were acclimatized for a week with ad libitum access to standard food and water under controlled temperature ($22 \pm 2$ °C) and humidity (45%−55%) conditions with a 12-h light/dark cycle.

The rats were given an intravenous (i.v.) injection of NC (2 mg/kg) in 20% ($m/V$) hydroxypropyl-β-cyclodextrin for the single-dose toxicokinetics study. The rats were euthanized with $CO_2$ gas, and their kidneys ($n = 3$) were collected before the dose and at 0.13, 0.5, 2, 8, 24, and 48 h after i.v. administration. The kidneys were snap-frozen in liquid nitrogen and then stored at −80 °C until analysis.

The rats were randomly assigned to the control group (Control, $n = 6$), low-NC group (L-NC, $n = 6$), and high-NC group (H-NC, $n = 6$) for the chronic nephrotoxicity study. The L-NC and H-NC groups received i.v. injections of NC at 2 and 6 mg/kg, respectively, in 20% ($m/V$) hydroxypropyl-β-cyclodextrin once daily for 21 days, while the control group was treated with 20% ($m/V$) hydroxypropyl-β-cyclodextrin. The animals' general state was observed daily during the treatment period, while their water and food consumption and body weight were monitored every four days. On day 21, after fasting overnight for 12 h, blood samples were collected from the angular vein and centrifuged at 4,000 r/min for 10 min at 4 °C to obtain serum. The rats were then euthanized with $CO_2$ gas, and their kidneys were immediately removed and snap-frozen in liquid nitrogen. All samples were stored at −80 °C until analysis. The Biological and Medical Ethics Committee of the Minzu University of China approved this study (Approval No.: 2017-01).

### 2.3. Biochemical analysis and hematoxylin and eosin (H&E) staining

The blood biochemical parameters, including blood urea nitrogen (BUN), serum creatinine (Bcr), uric acid (UA), glucose (GLU), total cholesterol (TC), and triglyceride (TG) levels, were measured using an AU5800 automatic chemistry analyzer (Beckman Coulter Inc., Brea, CA, USA).

Frozen renal sections (10 μm) were prepared at −20 °C on a CM1860 cryostat (Leica Microsystems Ltd., Wetzlar, Germany) and mounted onto adhesion with poly-ʟ-lysine microscope slides (Jiangsu Shitai experimental equipment Co., Ltd., Nantong, China). We examined the histopathological lesions of renal sections using H&E staining.

### 2.4. Sample preparation

The frozen kidney tissues were sectioned into 10-μm thick slices and mounted on adhesive microscope slides for AFADESI-MSI analysis. In addition, separate tissue sections were affixed to silicon wafers for ToF-SIMS analysis. These prepared sections were subsequently stored at −80 °C until analysis. Prior to conducting AFADESI-MSI and ToF-SIMS analyses, all sections underwent a 30-min vacuum-drying process at room temperature to eliminate any residual moisture.

### 2.5. AFADESI-MSI and ToF-SIMS analyses

AFADESI-MSI analysis was conducted using a lab-built AFADESI-MSI platform equipped with an AFADESI ambient ion source and a Q-OT-qIT hybrid mass spectrometer (Orbitrap Fusion Lumos; Thermo Fisher Scientific Inc., San Jose, CA, USA). Mass spectra were acquired in positive and negative full MS mode, with a scan range of 100−1000 Da, mass resolution of 120,000 full width at half maximum (FWHM) at $m/z$ 200. The kidney tissue sections were scanned at a moving rate of 0.2 mm/s in the $x$-step, and the vertical step in the $y$-step was 0.2 mm. Detailed parameter settings were presented (Table S1).

For ToF-SIMS analysis, we employed a ToF-SIMS V instrument (IONTOF GmbH, Muenster, Germany) equipped with a Bi liquid metal ion gun (LMIG). Tissue samples were subjected to ToF-SIMS spectra and imaging using a 30 keV $Bi_3^+$ LMIG with high spatial resolution (HSR) mode. A 10 keV $Ar_{2500}+$ commercial gas cluster ion gun served as the sputter gun (incident angle 45°) for depth profiling. Secondary ion images were acquired by rastering over a 500 μm × 500 μm area with a resolution of 256 × 256 pixels, encompassing 100 layers of depth profiling scans. In the HSR mode, the $Bi^{3+}$ current was maintained at 0.1 pA (with a 100 ns pulse width for unbunched beam). Throughout the experiment, the ion dose was kept below the static limit of $10^{13}$ ions/$cm^2$ to minimize the surface damage of the sample. A flood gun with low energy electrons was used to compensate for charge buildup on the sample surface.

### 2.6. Data processing and analysis

AFADESI-MSI data processing and analysis were conducted following the procedures outlined in our previous work. Briefly, we converted the raw files obtained from the analysis in the positive and negative AFADESI-MSI ion modes to .cdf format by Xcalibur 4.0.2 (Thermo Scientific, San Jose, CA USA). We constructed the ion image using custom-developed high-performance imaging software (MassImager 2.0, Beijing, China) with a bin width of $\Delta m/z = 0.005$. We extracted the average AFADESI-MS profiles from regions of interest (ROIs) by matching them with H&E stain images of the adjacent renal section, generating separate two-dimensional (2D) data matrixes ($m/z$ and intensity) in .txt format. After background deduction, peak picking, and peak alignment using Markerview™ software 1.2.1 (AB SCIEX, Toronto, Canada), total ion current normalization was used to calculate the relative intensity of ions in each ROI. Student's $t$-test analysis was performed among the control, the L-NC, and the H-NC groups to identify differential metabolites associated with nephrotoxicity. A statistically significant difference was defined as $P$-values $< 0.05$. The area under the curve (AUC) was calculated using GraphPad Prism 9.4. software (GraphPad Software, San Diego, CA, USA).

The ToF-SIMS images were acquired and saved using the built-in data processing software, SurfaceLab. Ion spectral peaks employed for MSI and data acquisition were chosen based on predetermined screening conditions, followed by mass correction and peak

identification. Each peak represents a highly spatially resolved and spectrally filtered ion image. The overlay of ion images was subsequently processed using ImageJ FIJI (v.1.53a).

### 2.7. LC-MS/MS analysis of metabolites of NC in kidney homogenates

Structural information for metabolites of NC was obtained through high-resolution LC-MS/MS analysis of kidney homogenates. Detailed procedures for the LC-MS/MS experiments are provided in the Supplementary data.

### 2.8. Metabolite identification

We initially calculated the possible element compositions of the ion using Xcalibur 4.0 (Thermo Fisher Scientific Inc.) based on exact mass (with mass accuracies < 5 ppm) and isotope patterns. These ions were then matched against the Human Metabolome Database (HMDB) (http://hmdb.ca/) [27], METLIN (http://metlin.scripps.edu/) [28], and a homemade metabolite library to find possible metabolites [22]. LC-MS/MS analyses of kidney tissue homogenates were performed to obtain structural information on these metabolites (Supplementary data).

## 3. Results and discussion

### 3.1. Chronic nephrotoxicity assessment of NC in rat

We presented kidney weight, kidney/body weight ratio, and representative photomicrographs of H&E-stained kidney tissues (Fig. 2). Left Kidney weight was significantly higher in the L-NC
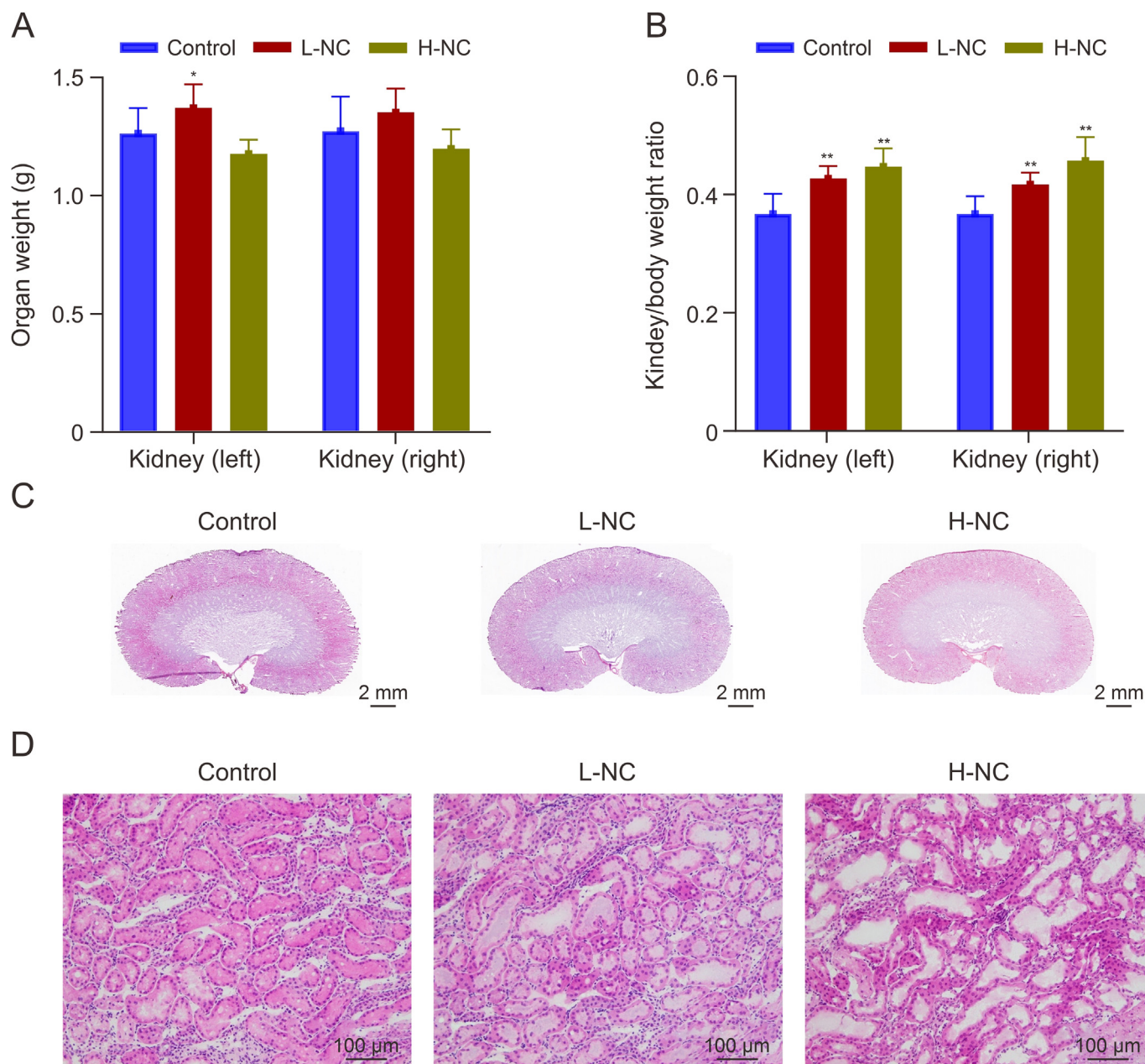


**Fig. 2.** Assessment of renal damage in nitidine chloride (NC)-treated rats. (A) Kidney weight. (B) Kidney/body weight ratio. (C) Hematoxylin and eosin (H&E) images of whole kidney sections of rats after 21-day repeated doses of NC. (D) H&E image of the renal cortex. L-NC: low-dose NC (2 mg/kg) group; H-NC: high-dose NC (6 mg/kg) group. Significance level compared to the control group, $^*P < 0.05$ and $^{**}P < 0.01$ (mean ± standard deviation, $n = 6$).
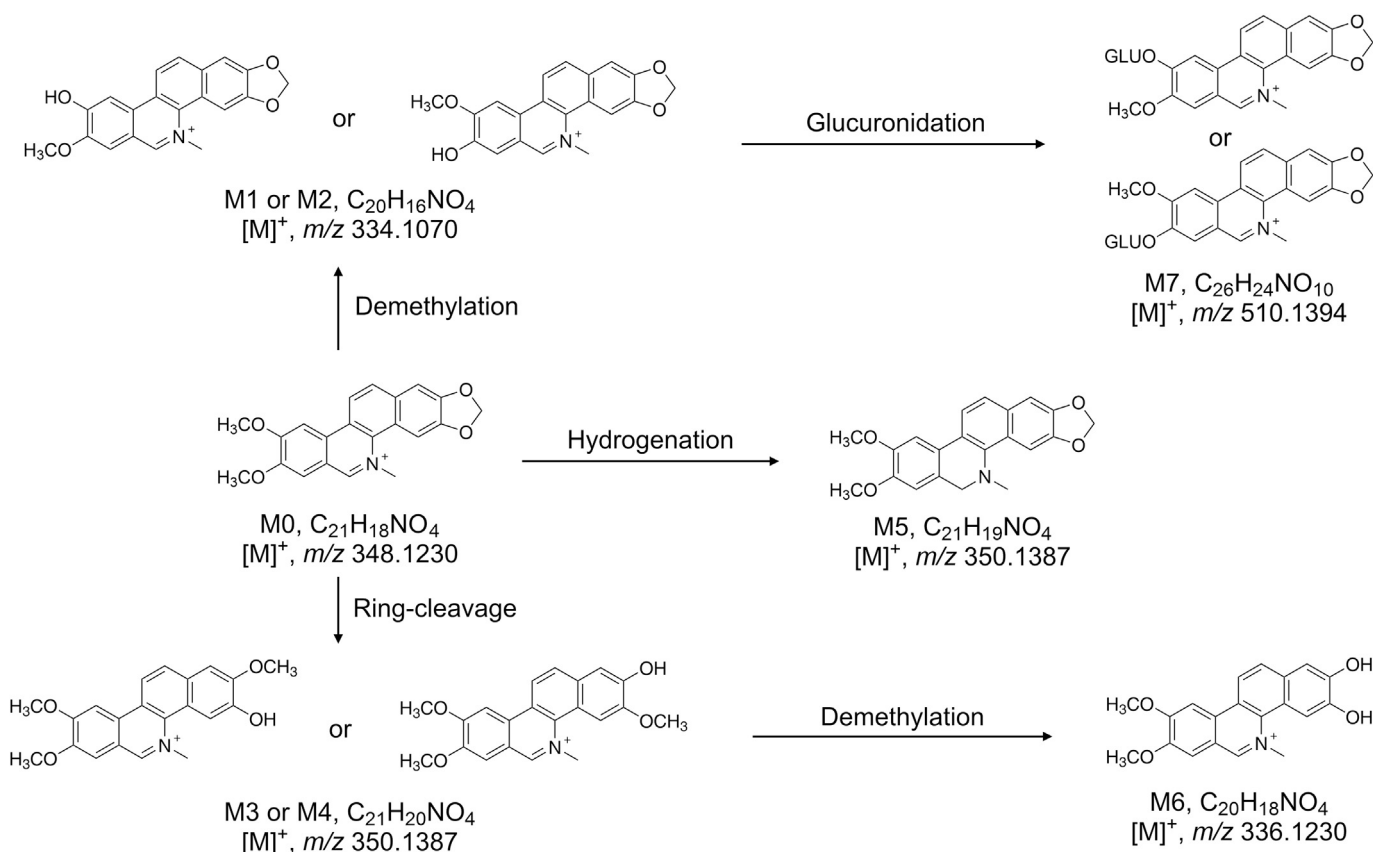
**Fig. 3.** Proposed metabolic pathway of nitidine chloride (NC) in rat kidneys. M0: NC; M1/M2: demethyl metabolites; M3/M4: ring-cleavaged metabolites; M5: dihydro metabolite; M6: dimethyl metabolite; and M7: glucuronic acid-conjugated metabolite. GLUO: glucuronidation.

group than in the control group (Fig. 2A). Kidney/body weight ratio was significantly higher in both the L-NC and H-NC groups compared to the control group (Fig. 2B). Histological examination of H&E-stained kidney tissues demonstrated diffuse dilatation of deep cortical renal tubules and protein flocculent material in the tubular lumen in rats of both the L-NC and H-NC groups (Figs. 2C and D). The above lesions in the kidney tissues of the H-NC group appeared heavier than those in the L-NC group, indicating a dose-dependent NC-induced nephrotoxicity in the rats.

Body weight, food consumption, and water consumption for rats in the control, L-NC, and H-NC groups are assessed and summarized (Fig. S1). These parameters showed no significant differences in the L-NC group compared to the control group, while the H-NC group rats exhibited reduced body weight and food consumption, indicating the overall toxicity of NC in rats. The blood and urinary biochemical indicators were depicted (Fig. S2). The concentrations of blood GLU were significantly increased ($P < 0.01$) in both the L-NC and H-NC groups (Fig. S2A). However, serum cholesterol levels were not significantly changed in either of the groups (Fig. S2B). TG and UA were significantly reduced (all $P < 0.01$) in both groups (Figs. S2C and D), while those of BUN and Bcr levels were significantly elevated (all $P < 0.01$) in the H-NC group (Figs. S2E and F).

In summary, the physiological, biochemical, and histopathological H&E staining results indicated that NC induced chronic nephrotoxicity in rats even at a repeated dose of 2 mg/kg for 21 days, which was lower than the dose in a previous study [14].

### 3.2. Identification of metabolites of NC in rat kidney

All possible metabolism patterns of NC, including hydroxylation, oxidation, dehydrogenation, cyclization, demethylation,

glucuronidation, sulfation, and others, were explored. The result identified seven metabolites, and their high-resolution LC-MS/MS data and chemical composition were provided (Fig. S3 and Table S2). These results indicated extensive NC metabolism in rat kidney, with six Phase I metabolites, including demethyl metabolites M1 ($[M]^+$, $m/z$ 334.1070) and M2 ($[M]^+$, $m/z$ 334.1070), ring-cleavaged metabolites M3 ($[M]^+$, $m/z$ 350.1387) and M4 ($[M]^+$, $m/z$ 350.1387), dihydro metabolite M5 ($[M+H]^+$, $m/z$ 350.1387), and ring-cleavaged and dimethyl metabolite M6 ($[M+H]^+$, $m/z$ 336.1230), one Phase II metabolite, and glucuronic acid-conjugated metabolite M7 ($[M]^+$, $m/z$ 510.1394) being detected in kidney tissue (Fig. 3). The potential fragmentation pathway of M0 (NC; $[M]^+$, $m/z$ 348.1230) was proposed and summarized (Fig. 4).

### 3.3. Optimization of conditions for AFADESI-MSI analysis

We optimized the key AFADESI-MSI platform parameters, including spray solvent selection and flow rate, using adjacent sections from half of the collected rat kidneys at 0.5 h after NC administration to enhance the *in situ* detection of metabolites of NC and the endogenous metabolites in the kidney. Three commonly used spray solvents, including MeOH/H$_2$O (8:2, *V/V*), ACN/H$_2$O (8:2, *V/V*), and IPA/H$_2$O (8:2, *V/V*), were evaluated. The results revealed that ACN/H$_2$O (8:2, *V/V*) had the highest ion response intensities for NC metabolites and endogenous metabolites (Fig. S4). We further compared the flow rate of the spray solvent at 5, 7, and 10 μL/min and revealed that 10 μL/min resulted in higher MS response intensities for most of the representative ions (Fig. S5). Therefore, we selected ACN/H$_2$O (8:2, *V/V*) at 10 μL/min for subsequent AFADESI-MSI analysis.
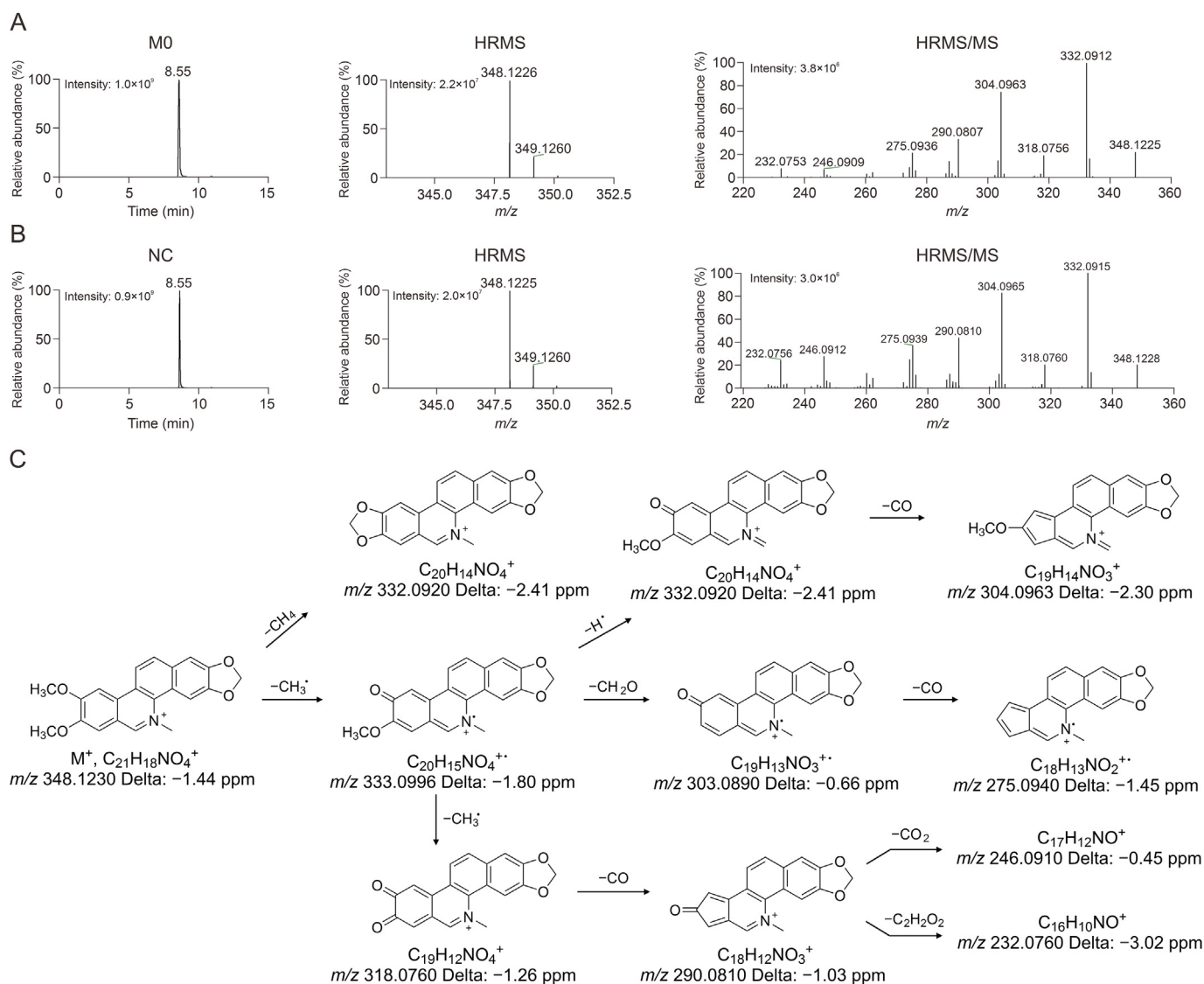
**Fig. 4.** The extracted ion chromatograms and possible fragmentation pathway of nitidine chloride (NC). (A) Extracted ion chromatograms, high resolution mass spectrometry (HRMS), and HRMS/MS spectra of the NC in kidney tissue. (B) Extracted ion chromatograms, HRMS, and HRMS/MS spectra of the NC standard. (C) Fragmentation pathway of NC. M0: NC.

Mass resolution is a critical factor that affects the specificity and sensitivity of the MSI method, especially for complex biological samples that contain a large number of metabolites having similar exact mass values. This study revealed that the $[M+2]^+$ isotope peak ($m/z$ 350.1297) of NC may significantly interfere with the detection of its ring-cleavaged metabolites (M3 and M4, $[M]^+$, $m/z$ 350.1387) and dihydro metabolite (M5, $[M+H]^+$, $m/z$ 350.1387) in AFADESI-MSI analysis due to the high concentration of NC relative to its metabolites. Therefore, we tested different MS resolutions (30,000, 60,000, 120,000, and 240,000 FWHM) to effectively separate NC from its metabolites. Increasing the MS resolution from 30,000 to 240,000 FWHM resulted in sharp separation between NC isotopes and its ring-cleavaged and dihydro metabolites by MS, thereby significantly improving the selectivity of the MS image (Figs. 5A and B). However, they could not be separated by AFADESI-MSI even with the highest MS resolution due to the same $m/z$ value of M3, M4, and M5. Additionally, increasing the MS resolution resulted in a decrease in scan speed in the Orbitrap instrument, which may affect the sensitivity of AFADESI-MSI analysis.

Therefore, we selected an MS resolution of 120,000 for the AFADESI-MSI analysis of NC metabolites, because it provided a good balance between specificity and sensitivity (Fig. S6).

We spotted 1 μL of the standard solutions of NC at concentrations of 0.15, 0.3, 0.6, 1, 3, 6, and 10 μg/mL on the blank kidney homogenate sections (the area of each point after droplet drying was approximately 4.97 mm$^2$) to further investigate the quantitative ability of the proposed method. The resulted densities of the standard NC at corresponding spots were 0.03, 0.06, 0.12, 0.20, 0.60, 1.20, and 2.00 ng/mm$^2$, respectively. Finally, these spots were subjected to AFADESI-MSI analysis. The standard curve was generated for NC by plotting the average ion intensities of the mass spectra in the defined ROIs as a function of the quantity of the standard spotted on the tissue sections. We successfully visualized NC at all concentrations by detecting the $[M]^+$ ion at $m/z$ 348.1230 (Fig. 5C). The calibration curve exhibited good linearity of 0.03−2.00 ng/mm$^2$ with a correlation coefficient ($R^2$) of 0.9956 ($n = 3$) (Fig. 5D). These results indicate that the proposed AFADESI-MSI method results in the production of concentration-dependent
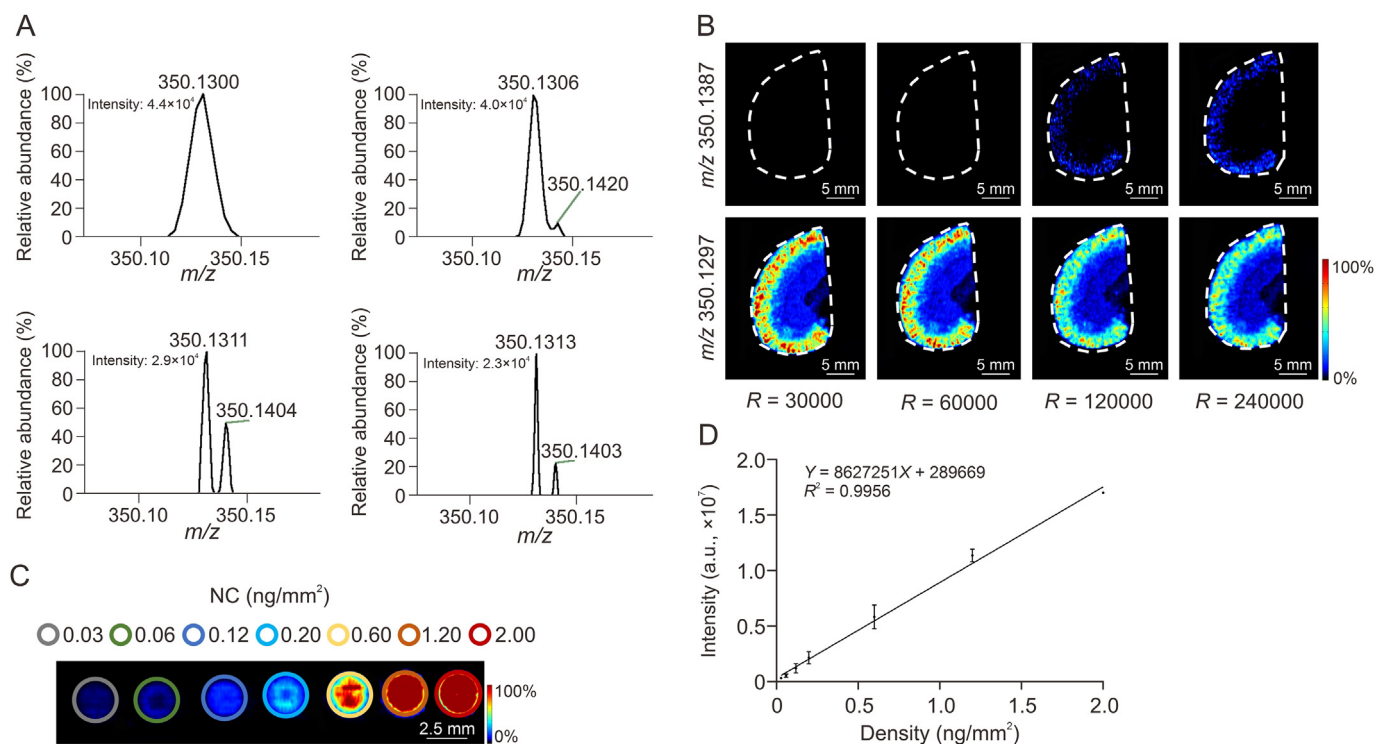
**Fig. 5.** Evaluation of specificity and linearity of the air flow-assisted desorption electrospray ionization mass spectrometry imaging (AFADESI-MSI) method. (A) AFADESI-MS spectra and images of $m/z$ 350.1387 and 350.1297 ions in rat kidney under different mass resolution. (B) AFADESI-MS image of $m/z$ 350.1387 and 350.1297. (C) AFADESI-MS images of standards of nitidine chloride (NC) ($m/z$ 348.1230) deposited on a blank kidney tissue homogenate section. (D) Standard curve of NC ($R^2 = 0.9956$, $n = 3$).

signals for NC and can be utilized to quantitively visualize NC in kidney sections.

We assessed the stability of the AFADESI-MSI system by analyzing adjacent renal slices over three successive days. Most of the relative standard deviation (RSD) of the relative intensities of representative metabolites were <15%, indicating that the reproducibility of the AFADESI-MSI approach was suitable for *in situ* analysis of metabolites of NC and the endogenous metabolites on kidney sections (Fig. S7).

### 3.4. Spatiotemporal distribution of NC and its metabolites in rat kidneys

We used the optimized AFADESI-MSI method to analyze the spatiotemporal distribution of NC and its metabolites in rat kidneys after a single and repeated dosing of NC. The coronal section of the kidney was roughly divided into six regions based on its anatomical structure and physiological function, including the whole renal section (W), outer cortex (OC), inner cortex (IC), outer medulla (OM), inner medulla (IM), and pelvis (P). We successfully detected NC and all of its metabolites, except for M7, in multiple regions of the kidney collected at different time points after dosing (Fig. 6A).

NC is more abundant than its metabolites in the kidney (Figs. 6A and S8), with its AUC accounting for >98% of the total AUC, indicating a low metabolism rate in rat kidneys. After a single dose administration, NC is detected in the kidney as early as 0.13h, indicating rapid distribution, with a predominant presence in the cortex region. NC is rapidly distributed in the OC region initially, but it gradually accumulates in the IC region over time and remains detectable up to 48 h after administration. M1/M2 is present in low amounts in the kidney and is widely distributed across the kidney, reaching a peak concentration in the P region at 0.13 h post-

administration, then declining and becoming undetectable 24 h afterward. This indicates that they are rapidly excreted in urine once they enter the kidney. The M1/M2 concentration decreased with time and was not detectable at 24 h after administration. In contrast, M3/M4/M5 are the most abundant metabolites of NC, mainly distributed in the renal cortex. Their concentration increases over time, reaching the highest concentration 8 h after administration. These metabolites remain detectable in the IC region 48 h after administration. M3, M4, and M5 cannot be separated by AFADESI-MSI, but they have different chromatographic retention times in LC-MS/MS analysis. We compared their relative concentrations based on their chromatographic peak areas and revealed that the concentration of M3 and M4 combined is approximately 7.68 times higher than that of M5 (Fig. S8B), and NC is more likely to undergo ring-cleavage metabolic reaction than hydrogenation metabolic reaction in the kidney. M6 was detected in low abundance in the kidney and was mainly distributed in the IC, with the highest concentration 8 h after administration. It remains detectable in the IC region 24 h after administration.

NC is highly abundant in the kidney, thus we performed a quantitative evaluation of its regional toxicokinetics (Fig. 6B). NC concentration in each kidney region was calculated using the equation obtained from the appropriate calibration curve. The time-concentration curve was then plotted to analyze the toxicokinetic behavior of NC in each kidney region. The time to maximum concentration ($t_{max}$) in OC, OM, and IM regions was 0.5 h, with the concentration maximum ($c_{max}$) values of $0.44 \pm 0.16$, $0.08 \pm 0.02$, and $0.04 \pm 0.01$ ng/mm$^2$, respectively (Table S3). In contrast, the $t_{max}$ is 8 h with a $c_{max}$ value of $0.55 \pm 0.24$ ng/mm$^2$ in the IC region. Additionally, the elimination rate of NC in the IC region was the slowest among all the regions, with a concentration of $0.16 \pm 0.10$ ng/mm$^2$ in IC in 48 h (Fig. 6B). Furthermore, the AUC of NC in IC, OC, OM, and IM regions accounted for 61.83%, 32.25%, 4.32%, and 1.60% of the
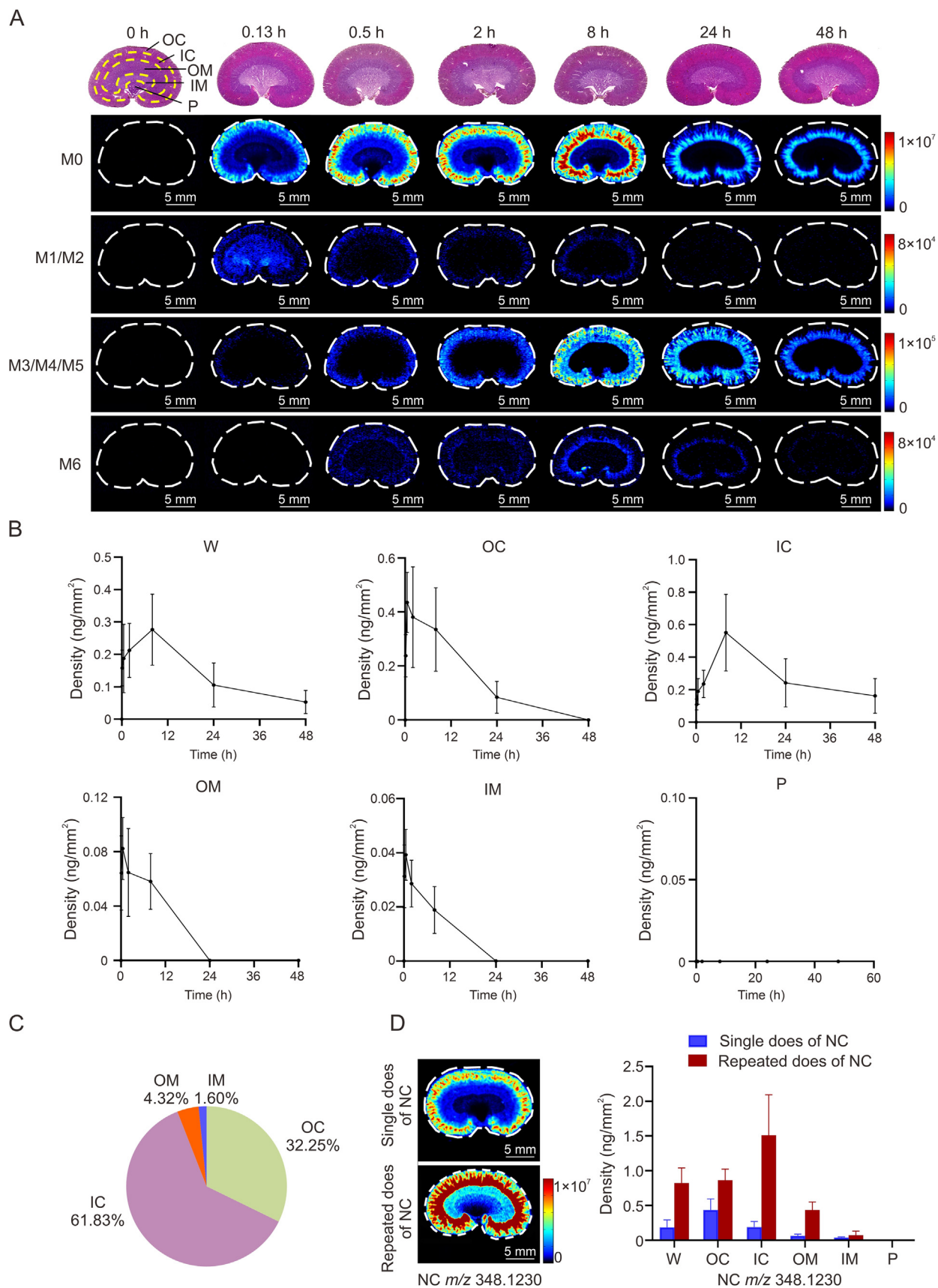
**Fig. 6.** Spatiotemporal alteration of nitidine chloride (NC) and its metabolites in rat kidneys. (A) Air flow-assisted desorption electrospray ionization mass spectrometry (AFADESI-MS) images of NC and its metabolites in the kidney. (B) NC concentration in the different kidney microregions. Data are presented as means ± standard deviation ($n = 3$). (C) The percentage of area under the curve (AUC) in NC in different kidney regions. (D) NC accumulation in different kidney regions after repeat dosing. OC: outer cortex; IC: inner cortex; OM: outer medulla; IM: inner medulla; P: papilla; M0: NC; M1/M2: demethyl metabolites; M3/M4: ring-cleavaged metabolites; M5: dihydro metabolite; M6: dimethyl metabolite; W: whole renal section.
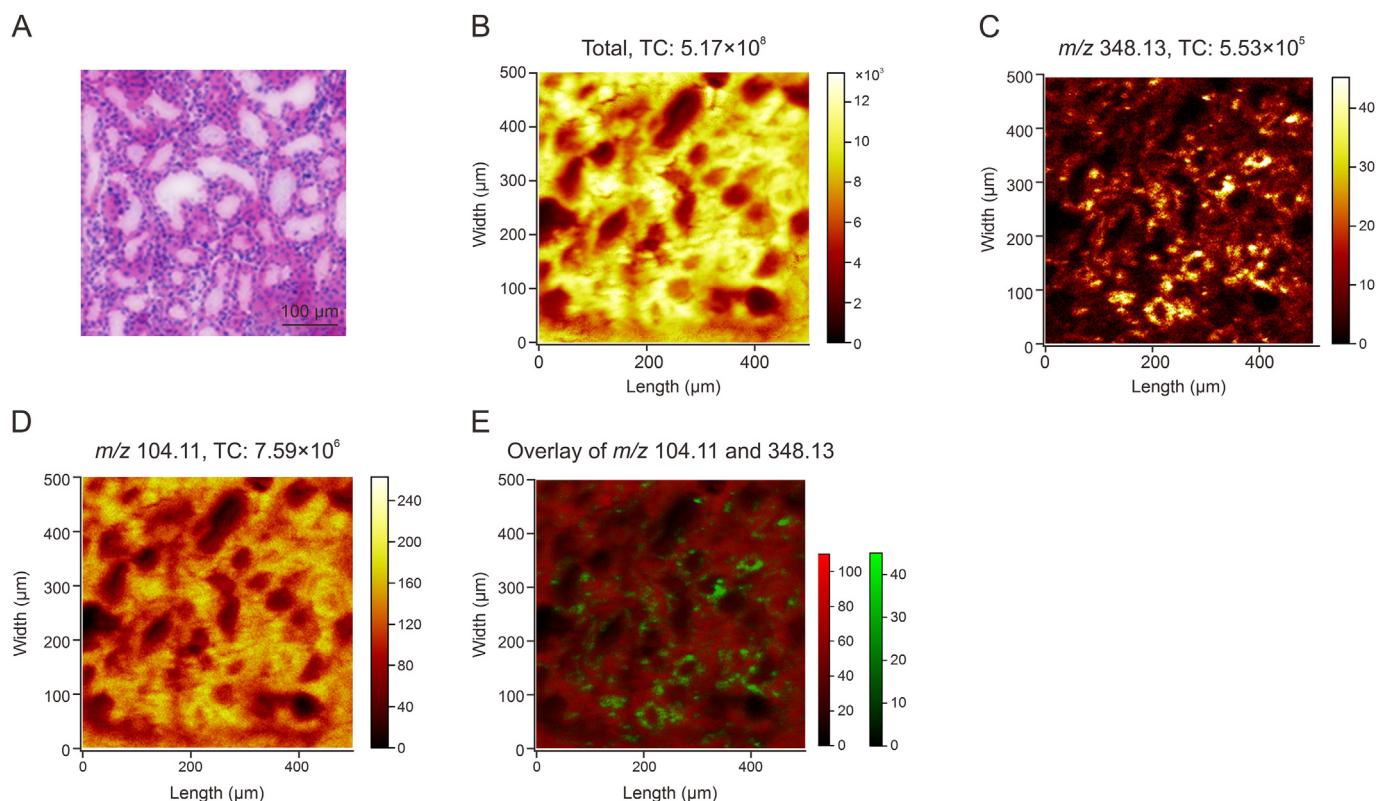
**Fig. 7.** Time-of-flight secondary ion mass spectrometry (ToF-SIMS) ion images of kidney tissue samples on glass slide. (A) Hematoxylin and eosin (H&E) images of the kidney sections of rats after 21-day repeated doses of nitidine chloride (NC). (B) Spatial characterizations of in the rat kidney. (C, D) Spatial distributions of $m/z$ 348.13 (C) and 104.11 (D). (E) The merged image of Figs. 7C and D. The green and red colors indicate the distributions of $m/z$ 348.13 and 104.11, respectively. The $m/z$ 104.11 could potentially correspond to fragments or ions related to phosphatidylcholine (PC), a class of phospholipids commonly found in cell membranes. The ToF-SIMS images were acquired at a spatial resolution of about 2 μm. TC: total ion count.

total AUC in the kidney (Fig. 6C). After repeated daily dosing for 21 days, the concentration of NC in the OC, IC, OM, and IM regions was found to be 1.98, 7.96, 6.62, and 1.80 times higher, respectively, compared to rats that received a single dose of NC, indicating a significant accumulation of NC in kidney, especially in the IC region (Fig. 6D).

To precisely locate NC within the IC region, we utilized high spatial resolution ToF-SIMS guided by H&E-stained kidney tissue in a positive mode. As illustrated in Fig. 7, NC ($m/z$ 348.13) was exclusively localized within the tubular walls, signifying substantial exposure of the renal tubular epithelium to NC, consistent with the observed kidney pathological lesions.

To summarize, based on the high exposure level, low elimination rate, accumulation of NC in the IC region, as well as the observed histopathological lesions in this area, it is reasonable to conclude that NC is likely the main substance responsible for its nephrotoxicity, and the IC region is likely the primary toxic target site of NC. The IC region mainly consists of proximal tubule cells, which express a variety of transporters, including organic cation transporters (OCTs), responsible for the uptake and elimination of both endogenous compounds and xenobiotics [14]. The region-specific enrichment of NC in the IC region may be attributed to its high affinity as a substrate of OCTs, specifically OCT2. Additionally, although M3/M4 are present in low concentration, their low elimination rate and significant accumulation in the IC region after repeated daily dosing for 21 days suggest their potential contribution to the nephrotoxicity of NC (Fig. S9). Furthermore, the phenolic hydroxyl groups present in their structure may have pro-oxidant properties, increasing their potential to contribute to the toxicity of NC.

### 3.5. Spatial metabolic alterations in NC-treated kidneys

The frozen renal sections from the control and L-NC/H-NC treated rats were analyzed by AFADESI-MSI to investigate the spatially resolved metabolic alteration in the kidneys. We detected 1508, 1504, 1290, 1497, 1386, and 1322 ion features in the W, OC, IC, OM, IM, and P regions in the positive AFADESI-MSI mode and 386, 374, 346, 327, 321, and 349 peaks in the negative AFADESI-MSI mode, respectively.

A Student's $t$-test was performed to compare the metabolic profiles of each kidney region between the control and NC-treated groups. We selected 424, 437, 350, 305, 407, and 253 differentiating variables in the W, OC, IC, OM, IM, and P regions of the L-NC group rats and 526, 413, 534, 447, 324, and 186 differentiating variables across different regions of the H-NC group rats, respectively. Additionally, we identified 18, 17, 15, 18, 9, and 3 differential endogenous metabolites across different regions in the L-NC group rats (Tables S4—S7) and 36, 33, 34, 30, 21, and 11 metabolites across different regions in the H-NC group rats, respectively. Among them, 35 metabolites were consistent with those identified in the L-NC group (Fig. S10A).

Our study used a systematic approach to investigate the regional metabolic alterations in rats that are subjected to chronic NC exposure, utilizing a highly sensitive AFADESI-MSI-based spatial metabolomic technique. This analysis determined 74 discriminating metabolites across various kidney regions in NC-treated rats. These metabolites included amino acids, organic acids, nucleotides and their derivatives, choline, carnitine, fatty acids (FAs) and their derivatives, and glycerophospholipid compounds (Figs. S10B and C). These findings reveal multiple metabolic pathways (Figs. S10D

and E), indicating significant metabolic changes within distinct kidney regions of NC-treated rats, particularly noticeable in the H-NC group.

### 3.5.1. Disturbance of lipid metabolism

The study revealed significant changes in FA metabolism in the kidney in the L-NC and H-NC groups (Figs. 8 and S11), and five polyunsaturated FAs (PUFAs), including timnodonic acid (FA (20:5)), arachidonic acid (FA (20:4)), epoxyeicosatrienoic acid (FA (20:3)), docosahexaenoic acid (FA (22:6)), and docosapentaenoic acid (FA (22:5)), were significantly reduced across the kidney sections of rats in the H-NC group, while only FA (20:4) and FA (20:3) were significantly reduced in the L-NC group. PUFAs play a crucial role in maintaining membrane fluidity and function and are the precursors of prostaglandins and leukotrienes. Additionally, PUFAs have demonstrated antioxidant properties and antifibrotic effects, because they can scavenge free radicals and reactive oxygen species (ROS), thereby reducing oxidative stress, inflammation, and extracellular matrix deposition in the body [29]. Decreased PUFA levels indicated that increased oxidative stress and inflammation may be happening in the kidneys of diabetic nephropathy rats [30,31].

Phospholipids have a variety of functions, including maintaining the normal structure and function of biofilms, participating in cellular information transmission, promoting fat and fat-soluble cellulose absorption and transportation, and transforming them into a variety of important bioactive substances. Our study revealed notable changes in the spatial distribution of several phospholipids, including phosphatidylcholine (PC), phosphatidylethanolamine (PE), phosphatidylinositol (PI), phosphatidylglycerol (PG), phosphatidic acid (PA), phosphatidylserine (PS), and diacylglycerol (DG), in the NC-treated kidney (Figs. 8 and S11−S13). PC (32:0), PC (34:1), PC (34:2), PC (36:2), PC (38:4), PC (38:6), lysophosphatidylcholine (Lyso PC) (16:0), Lyso PC (20:4), and Lyso PC (18:1) were significantly elevated in the rat kidney in the H-NC group, particularly evident in the IC and OM regions (Fig. 8). Lyso PC (16:0) and Lyso PC (18:0) were significantly elevated in the rat kidney in the L-NC group. PE (36:4), PE (36:4-OH), PE (36:2), PE (36:1), PE (38:5), and PE (38:4) were significantly accumulated in the rat kidney in the NC-treated group. PC and PE are the principal phospholipids in mammalian cell membranes. Alterations in the composition of these lipids affect the fluidity and permeability of the cell membranes. Such changes can subsequently influence the function of membrane proteins, such as receptors, ion channels, and transporters, which might affect drug uptake, efflux, and cellular responses, contributing to potential drug-induced toxic effects [32,33]. Additionally, previous studies have demonstrated that PC accumulation can enhance oxidative stress and inflammation [34]. LysoPC, a byproduct of PC metabolism, orchestrated by the enzyme phospholipase A2, can stimulate chemokine expression and molecule adhesion in glomerular cells. This can initiate macrophage activation and inflammation [35]. Moreover, elevated plasma levels of LysoPC have been associated with drug-induced nephrotoxicity [36].

### 3.5.2. Disturbance of carnitine metabolism

We observed a significant alteration of functional metabolites related to carnitine metabolism (Figs. 9 and S14). L-Carnitine showed a significant decrease in the kidney of the H-NC group, while acyl-carnitine (L-carnitine C2:0 and L-carnitine C18:0) demonstrated significant accumulation in the L-NC and H-NC groups, and 3-hydroxybutyrylcarnitine (AC4-OH; a FA β-oxidation intermediate) and 5-amino valeric acid betaine (5-AVAB) were significantly elevated in the H-NC group. L-carnitine serves as an essential intermediary in the transport of FAs to the mitochondria, where they undergo β-oxidation for adenosine triphosphate (ATP)

production [37,38]. Additionally, L-carnitine helps in removing potentially harmful acyl groups from cells and maintaining an appropriate ratio of coenzyme A within mitochondria, thereby indirectly contributing to antioxidant activities [39,40]. The kidneys play a crucial role in maintaining carnitine balance in the body. They reabsorb carnitine from the glomerular filtrate in the renal proximal tubules, thereby preventing its loss in urine [41]. The OCT2 is crucial in this process. The observed L-carnitine level reduction in the H-NC group indicates that a high dosage of NC might impede the OCT2 function. This could potentially increase the excretion of carnitine through urine, consequently resulting in a systemic deficiency of carnitine. Moreover, the combined L-carnitine depletion and accumulation of its derivatives indicate impaired mitochondrial functionality and a decreased capacity for FA oxidation, which could be detrimental to cellular health and overall metabolic balance [42,43].

### 3.5.3. Disturbance of arginine metabolism

Functional metabolites related to arginine metabolism showed a significant alteration (Figs. 10 and S15). The concentration of dimethylarginine and arginine was significantly decreased in rat kidneys in the L-NC and H-NC groups. Moreover, the dimethylarginine/arginine ratio (Fig. S15C) was significantly decreased in a dose-dependent manner in the IC region in L-NC and H-NC groups. In contrast, the creatine was significantly increased in rat kidneys in the L-NC and H-NC groups, especially in the cortex of the kidney. Arginine is involved in various metabolic processes, including immune function, protein metabolism, and wound healing [44,45]. It is also the sole precursor of nitric oxide (NO), which plays a role in immune and vascular regulation [46]. Arginine can be metabolized to dimethylarginine through the action of the enzyme, protein arginine N-methyltransferase (PRMT) [47]. Dimethylarginine is an endogenous inhibitor of NO synthase (NOS), which is the enzyme responsible for NO production. Decreased arginine and dimethylarginine levels indicate increased NO production, which may have detrimental effects on the kidney, including nitrative stress, oxidative stress, inflammation, and cellular damage [48,49]. A decreased dimethylarginine/arginine ratio in the IC region might indicate a potential reduction in PRMT activity. PRMT, which is involved in the methylation of arginine residues on target proteins, is crucial in diverse cellular processes such as transcriptional regulation, signal transduction, RNA processing, and DNA repair [50,51]. PRMT dysregulation has been associated with a variety of diseases, including cancer, cardiovascular disease, neurological disorders, and drug toxicity [52−54]. Consequently, PRMTs are being explored as potential targets for anti-cancer drug development [55]. The inhibitory effect of NC on PRMT could be part of the mechanism behind its anti-tumor effects.

Arginine can also be transformed into creatine and inosine through a series of enzymatic reactions [56]. Creatine serves as a substrate for OCTs and MATE transporters in the kidney [57]. These transporters play a crucial role in regulating blood concentrations of creatine, as well as eliminating the excess amounts from the body. Creatinine accumulation in the renal cortex indicates impaired clearance of the compound, potentially because NC inhibits OCT2 and MATE transporters. The buildup of creatine in the renal cortex may potentially cause various adverse effects, such as renal dysfunction, oxidative stress, and inflammation [58]. Furthermore, excessive creatine accumulation in the body may cause creatine kinase deficiency, resulting in muscular and neurological disorders [59,60].

### 3.5.4. Disturbance of choline metabolism

The spatial distribution of choline and its metabolites in rat kidneys is illustrated (Figs. S16 and S17). Choline is primarily
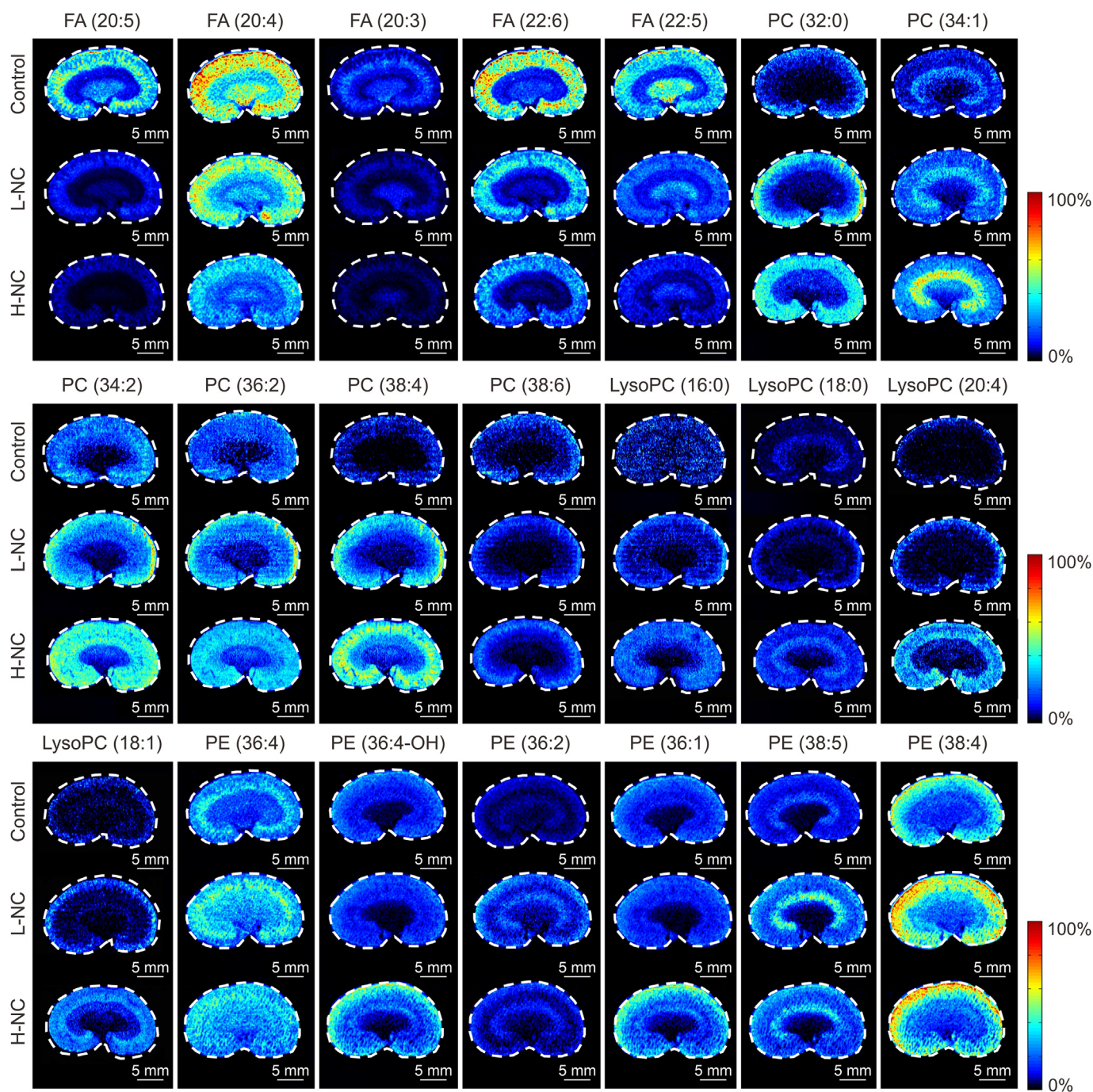
**Fig. 8.** Air flow-assisted desorption electrospray ionization mass spectrometry (AFADESI-MS) images of metabolites that are involved in lipid metabolism in rat kidneys of the control, low-dose nitidine chloride (2 mg/kg) (L-NC), and high-dose NC (6 mg/kg) (H-NC) groups. FA: fatty acid; PC: phosphatidylcholine; LysoPC: lysophosphatidylcholine; PE: phosphatidyl ethanolamine.

involved in the synthesis of PC, a major constituent of cell membranes. Betaine is a metabolite of choline oxidation, while glycerophosphocholine is a metabolite of choline phosphorylation. These metabolites play a role in maintaining electrolyte balance and axial osmolality gradient in the kidneys [61]. Furthermore, choline, betaine, and glycerophosphocholine are substrates for OCTs. Choline is significantly increased in the OC and IC regions in the L-NC group, and glycerophosphocholine is significantly increased in the P region in the H-NC group. Whereas betaine is significantly decreased in the OC and IC regions in the L-NC and H-NC groups. These results indicated that NC exposure even at a low dose (2 mg/kg) disrupts electrolyte balance and axial osmolality gradient in the kidney, which may be associated with OCTs dysfunction [25,61].

*3.5.5. Analysis of the correlation between metabolic alterations and NC exposure*

We performed correlation analyses between regional NC exposure and its metabolic effects to evaluate the dose-effect relationship in the targeted areas, including the IC and OC regions. The Pearson's correlation coefficients ($r$) between NC and discriminating metabolites are presented (Figs. S18 and S19).
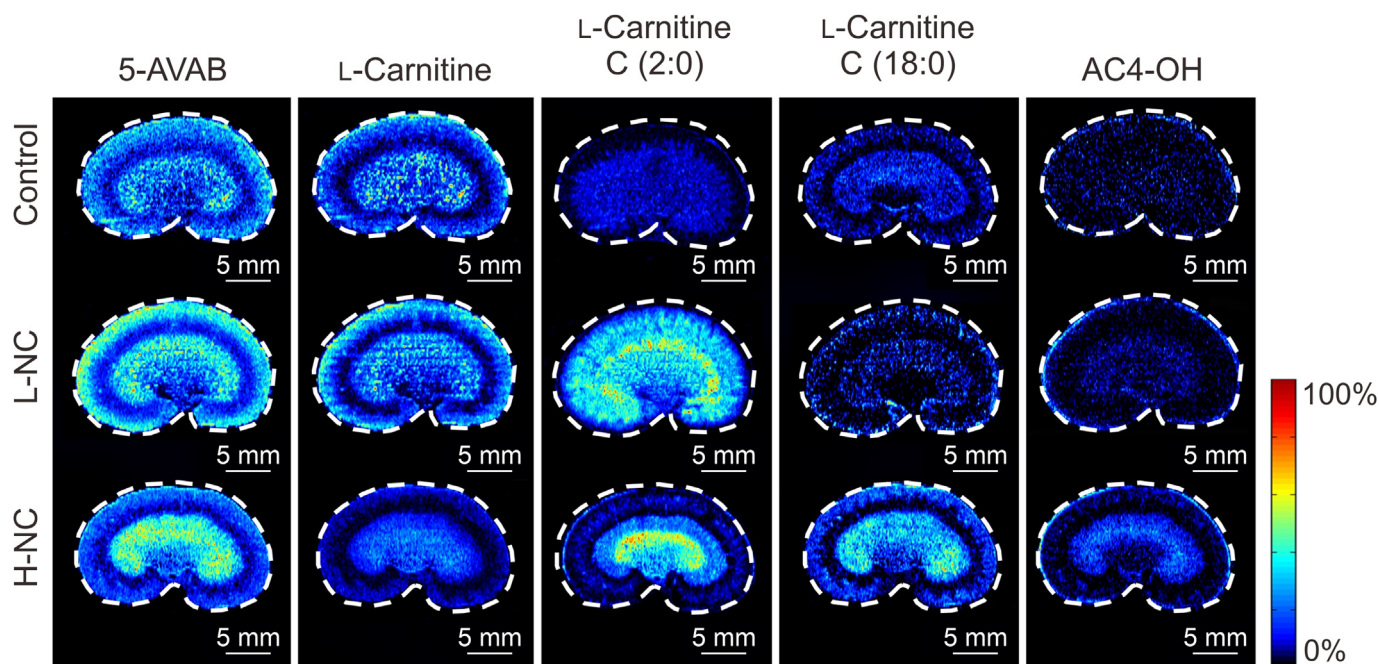
**Fig. 9.** Air flow-assisted desorption electrospray ionization mass spectrometry (AFADESI-MS) images of metabolites that are involved in carnitine metabolism in rat kidneys of the control, low-dose nitidine chloride (2 mg/kg) (L-NC), and high-dose NC (6 mg/kg) (H-NC) groups. 5-AVAB: 5-amino valeric acid betaine; AC4-OH: 3-hydroxybutyrylcarnitine.
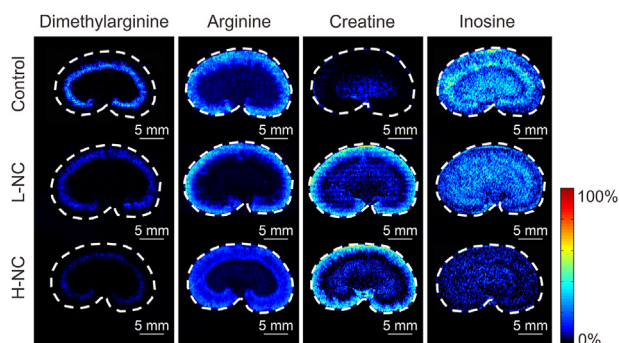


**Fig. 10.** Air flow-assisted desorption electrospray ionization mass spectrometry (AFADESI-MS) images of metabolites that are involved in arginine metabolism in rat kidneys of the control, low-dose nitidine chloride (2 mg/kg) (L-NC), and high-dose NC (6 mg/kg) (H-NC) groups.

We observed that 20 metabolites, including phosphoethanolamine, glutamate, citric acid, cholesterol sulfate, PC (38:4), PC (38:5), PC (40:6), LysoPI (18:0), LysoPI (20:4), PA (38:4), PE (36:4), PE (36:4-OH), PE (36:2), PE (36:1), PE (38:5), PE (38:4), PG (34:1), PI (34:0), PI (36:2), and PI (38:4), showed a strong positive correlation ($r \geq 0.6$) with NC in the IC region. Conversely, five metabolites, including betaine, taurine, dimethylarginine, xanthine, and pantothenic acid, exhibited a strong negative correlation ($r \leq -0.6$) with NC. In the OC region, 22 metabolites, including phosphoethanolamine, glutamate, ascorbic acid, citric acid, cytidine, glycerylphosphorylethanolamine, cholesterol sulfate, acylcarnitine C18:0, PC (38:4), LysoPG (18:1), LysoPI (18:0), LysoPI (20:4), PA (38:4), PE (36:4), PE (36:4-OH), PE (36:2), PE (38:5), PE (38:4), PS (38:4), PI (34:0), PI (38:4), and PI (40:6), demonstrated a strong positive association ($r \geq 0.6$) with NC. Conversely, histidine, arginine, L-carnitine, and FA (20:3) showed a strong negative correlation ($r \leq -0.6$) with NC.

The strong correlations between NC exposure and specific metabolites in both the IC and OC regions of the kidney not only elucidated the underlying toxic mechanisms of NC but also indicated these metabolites as unique, tissue-specific markers of NC-induced kidney damage. Moreover, conducting further studies on these markers with targeted and sensitive methods could help discover similar biomarkers in blood or urine, especially in larger animal studies. In particular, a metabolite, such as PC (38:4), tends to build up in the OC region in NC-induced kidney damage. This causes higher levels of this metabolite in the blood and lower levels in the urine. Conversely, a metabolite, such as betaine, decreases in the IC region in NC-induced kidney damage, causing lower levels in the blood and higher levels in the urine. These unique metabolic indicators could become a practical tool to monitor potential kidney damage caused by NC and other herbal medications that contain NC, in a clinical setting.

The current study has certain limitations. Specifically, we did not assess the pharmacokinetics (PK) of NC in serum during this investigation. However, it is essential to note that the PK of NC is well-documented [62], and our deliberate focus was on elucidating the regional toxicokinetics and toxicodynamics within rat kidneys. While the quantitation performance of the proposed AFADESI-MSI method for *in situ* detection of NC in the kidney has not undergone full validation, the method exhibits promising sensitivity and dynamic range. Notably, it successfully visualized NC at a concentration of 0.03 ng/mm$^2$ on renal sections and kidneys collected 48 h after a single dose administration, and it demonstrates concentration-dependent signals for NC within the range of 0.03−2.00 ng/mm$^2$. These encouraging results underscore the potential of AFADESI-MSI in exploring spatially resolved metabolic changes within intricate biological tissues. As we commit to future comprehensive validation efforts, these strengths position our study as a valuable contribution to understanding regional toxicological responses in the context of NC exposure.

## 4. Conclusion

This study introduced an integrated approach that combines AFADESI-MSI, ToF-SIMS, and spatial metabolomics to

comprehensively investigate the nephrotoxic effects induced by NC. This innovative approach offered high sensitivity, specificity, and spatial resolution, enabling us to simultaneously visualize region-specific toxicokinetics and toxicodynamics of NC across renal sections. Our findings shed light on the central role of the NC prototype, as opposed to its metabolites, in driving nephrotoxicity. This impact was particularly evident in the IC region and renal tubule epithelial cells, attributed to the substantial accumulation of NC in these areas. Furthermore, our results highlight the extensive interplay between NC and endogenous metabolites, revealing over 70 tissue-specific metabolites associated with NC exposure. This implicates renal transporters (such as OCTs, MATE, and OCT2), metabolic enzyme (such as PRMT and NOS), mitochondrial, oxidative stress, and inflammation in the pathogenesis of NC-induced nephrotoxicity. These metabolic markers could serve as crucial tools in devising more focused and efficient treatment strategies, thereby helping in reducing harm and maximizing the benefits of NC as an anti-cancer drug. In summary, our study elucidates the molecular mechanisms and target sites that are involved in NC-induced nephrotoxicity. The method that we used could be utilized as a template for similar studies that investigated the toxicity of other substances.

## CRediT author statement

**Shu Yang:** Methodology, Investigation, Visualization, Formal analysis, Writing - Original draft preparation; **Zhonghua Wang:** Conceptualization, Investigation, Supervision, Funding acquisition, Writing - Original draft preparation, Reviewing and Editing; **Yanhua Liu** and **Xin Zhang:** Investigation, Formal analysis; **Hang Zhang:** Investigation, Resources; **Zhaoying Wang** and **Zhi Zhou:** Methodology, Resources; **Zeper Abliz:** Conceptualization, Supervision, Funding acquisition, Writing - Reviewing and Editing.

## Declaration of competing interest

The authors declare that there are no conflicts of interest.

## Acknowledgments

## Appendix A. Supplementary data

Supplementary data to this article can be found online at https://doi.org/10.1016/j.jpha.2024.01.012.

## References

[1] Q. Lu, R. Ma, Y. Yang, et al., *Zanthoxylum nitidum* (Roxb.) DC: Traditional uses, phytochemistry, pharmacological activities and toxicology, J. Ethnopharmacol. 260 (2020), 112946.

[2] J. Hu, W. Zhang, R. Liu, et al., Benzophenanthridine alkaloids from *Zanthoxylum nitidum* (Roxb.) DC, and their analgesic and anti-inflammatory activities, Chem. Biodivers. 3 (2006) 990−995.

[3] N. Yang, R. Yue, J. Ma, et al., Nitidine chloride exerts anti-inflammatory action by targeting Topoisomerase I and enhancing IL-10 production, Pharmacol. Res. 148 (2019), 104368.

[4] J. Bouquet, M. Rivaud, S. Chevalley, et al., Biological activities of nitidine, a potential anti-malarial lead compound, Malar. J. 11 (2012), 67.

[5] Q. Lu, C. Li, G. Wu, Insight into the inhibitory effects of *Zanthoxylum nitidum* against *Helicobacter pylori* urease and jack bean urease: Kinetics and mechanism, J. Ethnopharmacol. 249 (2020), 112419.

[6] G. Yang, D. Chen, Alkaloids from the roots of *Zanthoxylum nitidum* and their antiviral and antifungal effects, Chem. Biodivers. 5 (2008) 1718−1722.

[7] L. Liu, D. Xiong, P. Lin, et al., DNA topoisomerase 1 and 2A function as

[8] oncogenes in liver cancer and may be direct targets of nitidine chloride, Int. J. Oncol. 53 (2018) 1897−1912.

[8] J. Chen, J. Wang, L. Lin, et al., Inhibition of STAT3 signaling pathway by nitidine chloride suppressed the angiogenesis and growth of human gastric cancer, Mol. Cancer Ther. 11 (2012) 277−287.

[9] M. Sun, N. Zhang, X. Wang, et al., Hedgehog pathway is involved in nitidine chloride induced inhibition of epithelial-mesenchymal transition and cancer stem cells-like properties in breast cancer cells, Cell Biosci. 6 (2016), 44.

[10] F. Ding, T. Liu, N. Yu, et al., Nitidine chloride inhibits proliferation, induces apoptosis via the Akt pathway and exhibits a synergistic effect with doxorubicin in ovarian cancer cells, Mol. Med. Rep. 14 (2016) 2853−2859.

[11] H. Xu, T. Cao, X. Zhang, et al., Nitidine chloride inhibits SIN1 expression in osteosarcoma cells, Mol. Ther. Oncolytics 12 (2019) 224−234.

[12] L. Li, M. Tu, X. Yang, et al., The contribution of human OCT1, OCT3, and CYP3A4 to nitidine chloride-induced hepatocellular toxicity, Drug Metab, Dispos. 42 (2014) 1227−1234.

[13] Y. Hong, W. Xu, J. Feng, et al., Nitidine chloride induces cardiac hypertrophy in mice by targeting autophagy-related 4B cysteine peptidase, Acta Pharmacol. Sin. 44 (2023) 561−572.

[14] L. Li, F.F. Song, Y.Y. Weng, et al., Role of OCT2 and MATE1 in renal disposition and toxicity of nitidine chloride, Br. J. Pharmacol. 173 (2016) 2543−2554.

[15] C.B. Lietz, E. Gemperline, L. Li, Qualitative and quantitative mass spectrometry imaging of drugs and metabolites, Adv. Drug Deliv. Rev. 65 (2013) 1074−1085.

[16] J. He, C. Sun, T. Li, et al., A sensitive and wide coverage ambient mass spectrometry imaging method for functional metabolites based molecular histology, Adv. Sci. (Weinh.) 5 (2018), 1800250.

[17] D. Liu, J. Huang, S. Gao, et al., A temporo-spatial pharmacometabolomics method to characterize pharmacokinetics and pharmacodynamics in the brain microregions by using ambient mass spectrometry imaging, Acta Pharm. Sin. B 12 (2022) 3341−3353.

[18] B. Jin, X. Pang, Q. Zang, et al., Spatiotemporally resolved metabolomics and isotope tracing reveal CNS drug targets, Acta Pharm. Sin. B 13 (2023) 1699−1710.

[19] E.M. Wans, M.M. Ahmed, A.A. Mousa, et al., Ameliorative effects of corn silk extract on acetaminophen-induced renal toxicity in rats, Environ. Sci. Pollut. Res. Int. 28 (2021) 1762−1774.

[20] F. Jia, X. Zhao, Y. Zhao, Advancements in ToF-SIMS imaging for life sciences, Front. Chem. 11 (2023), 1237408.

[21] A.V. Bensussan, J. Lin, C. Guo, et al., Distinguishing non-small cell lung cancer subtypes in fine needle aspiration biopsies by desorption electrospray ionization mass spectrometry imaging, Clin. Chem. 66 (2020) 1424−1433.

[22] Y. Zhu, Q. Zang, Z. Luo, et al., An organ-specific metabolite annotation approach for ambient mass spectrometry imaging reveals spatial metabolic alterations of a whole mouse body, Anal. Chem. 94 (2022) 7286−7294.

[23] K. Qi, L. Wu, C. Liu, et al., Recent advances of ambient mass spectrometry imaging and its applications in lipid and metabolite analysis, Metabolites 11 (2021), 780.

[24] Y. Lin, K. Wu, F. Jia, et al., Single cell imaging reveals cisplatin regulating interactions between transcription (co)factors and DNA, Chem. Sci. 12 (2021) 5419−5429.

[25] Z. Wang, B. He, Y. Liu, et al., *In situ* metabolomics in nephrotoxicity of aristolochic acids based on air flow-assisted desorption electrospray ionization mass spectrometry imaging, Acta Pharm. Sin. B 10 (2020) 1083−1093.

[26] C.B.A. Stoffels, T.B. Angerer, H. Robert, et al., Lipidomic profiling of PFOA-exposed mouse liver by multi-modal mass spectrometry analysis, Anal. Chem. 95 (2023) 6568−6576.

[27] D.S. Wishart, Y.D. Feunang, A. Marcu, et al., HMDB 4.0: The human metabolome database for 2018, Nucleic Acids Res 46 (2018) D608−D617.

[28] C.A. Smith, G. O'Maille, E.J. Want, et al., METLIN: A metabolite mass spectral database, Ther. Drug Monit. 27 (2005) 747−751.

[29] Z. Zeng, H. Yang, Y. Wang, et al., Omega-3 polyunsaturated fatty acids attenuate fibroblast activation and kidney fibrosis involving MTORC2 signaling suppression, Sci. Rep. 7 (2017), 46146.

[30] Z. Wang, W. Fu, M. Huo, et al., Spatial-resolved metabolomics reveals tissue-specific metabolic reprogramming in diabetic nephropathy by using mass spectrometry imaging, Acta Pharm. Sin. B 11 (2021) 3665−3677.

[31] H. Shapiro, M. Theilla, J. Attal-Singer, et al., Effects of polyunsaturated fatty acid consumption in diabetic nephropathy, Nat. Rev. Nephrol. 7 (2011) 110−121.

[32] J.N. van der Veen, J.P. Kennelly, S. Wan, et al., The critical role of phosphatidylcholine and phosphatidylethanolamine metabolism in health and disease, Biochim. Biophys. Acta Biomembr. 1859 (2017) 1558−1572.

[33] T. Xu, X. Xu, L. Zhang, et al., Lipidomics reveals serum specific lipid alterations in diabetic nephropathy, Front. Endocrinol. 12 (2021), 781417.

[34] F. Yang, L. Ren, L. Zhuo, et al., Involvement of oxidative stress in the mechanism of triptolide-induced acute nephrotoxicity in rats, Exp. Toxicol. Pathol. 64 (2012) 905−911.

[35] S.M. Lam, Y. Wang, B. Li, et al., Metabolomics through the lens of precision cardiovascular medicine, J. Genet. Genom. 44 (2017) 127−138.

[36] Y. Li, H. Deng, L. Ju, et al., Screening and validation for plasma biomarkers of nephrotoxicity based on metabolomics in male rats, Toxicol. Res. 5 (2016) 259−267.

[37] M.M. Adeva-Andany, I. Calvo-Castro, C. Fernández-Fernández, et al., Significance of l-carnitine for human health, IUBMB Life 69 (2017) 578−594.

[38] N. Longo, M. Frigeni, M. Pasquali, Carnitine transport and fatty acid oxidation, Biochim. Biophys. Acta 1863 (2016) 2422−2435.

[39] J. Liu, E. Head, H. Kuratsune, et al., Comparison of the effects of L-carnitine and acetyl-L-carnitine on carnitine levels, ambulatory activity, and oxidative stress biomarkers in the brain of old rats, Ann. N Y Acad. Sci. 1033 (2004) 117−131.

[40] T. Ulinski, M. Cirulli, M.A. Virmani, The role of L-carnitine in kidney disease and related metabolic dysfunctions, Kidney Dial. 3 (2023) 178−191.

[41] J. Pekala, B. Patkowska-Sokoła, R. Bodkowski, et al., L-Carnitine: Metabolic functions and meaning in humans life, Curr. Drug Metab. 12 (2011) 667−678.

[42] R.J.A. Wanders, G. Visser, S. Ferdinandusse, et al., Mitochondrial fatty acid oxidation disorders: Laboratory diagnosis, pathogenesis, and the complicated route to treatment, J. Lipid Atheroscler. 9 (2020) 313−333.

[43] S. Illsinger, N. Janzen, S. Sander, et al., Preeclampsia and HELLP syndrome: Impaired mitochondrial function in umbilical endothelial cells, Reprod, Sci. 17 (2010) 219−226.

[44] C. Baylis, Arginine, arginine analogs and nitric oxide production in chronic kidney disease, Nat. Clin. Pract. Nephrol. 2 (2006) 209−220.

[45] C.R. Martens, J.M. Kuczmarski, S. Lennon-Edwards, et al., Impaired L-arginine uptake but not arginase contributes to endothelial dysfunction in rats with chronic kidney disease, J. Cardiovasc. Pharmacol. 63 (2014) 40−48.

[46] G. Wu, S.M. Morris Jr., Arginine metabolism: Nitric oxide and beyond, Biochem. J. 336 (1998) 1−17.

[47] D. Tsikas, Urinary dimethylamine (DMA) and its precursor asymmetric dimethylarginine (ADMA) in clinical medicine, in the context of nitric oxide (NO) and beyond, J. Clin. Med. 9 (2020), 1843.

[48] M.D. Fulton, T. Brown, Y.G. Zheng, The biological axis of protein arginine methylation and asymmetric dimethylarginine, Int. J. Mol. Sci. 20 (2019), 3322.

[49] A.E. El-Sadek, E.G. Behery, A.A. Azab, et al., Arginine dimethylation products in pediatric patients with chronic kidney disease, Ann. Med. Surg. 9 (2012) (2016) 22−27.

[50] E. Guccione, S. Richard, The regulation, functions and clinical relevance of arginine methylation, Nat. Rev. Mol. Cell Biol. 20 (2019) 642−657.

[51] R.S. Blanc, S. Richard, Arginine methylation: The coming of age, Mol. Cell 65 (2017) 8−24.

[52] E. Smith, W. Zhou, P. Shindiapina, et al., Recent advances in targeting protein arginine methyltransferase enzymes in cancer therapy, Expert Opin. Ther. Targets 22 (2018) 527−545.

[53] B.Y. Ahn, M.H. Jeong, J.H. Pyun, et al., PRMT7 ablation in cardiomyocytes causes cardiac hypertrophy and fibrosis through β-catenin dysregulation, Cell. Mol. Life Sci. 79 (2022), 99.

[54] A. Jeong, Y. Cho, M. Cho, et al., PRMT7 inhibitor SGC8158 enhances doxorubicin-induced DNA damage and its cytotoxicity, Int. J. Mol. Sci. 23 (2022), 12323.

[55] J.W. Hwang, Y. Cho, G.U. Bae, et al., Protein arginine methyltransferases: Promising targets for cancer therapy, Exp. Mol. Med. 53 (2021) 788−808.

[56] S. Benito, A. Sánchez, N. Unceta, et al., LC-QTOF-MS-based targeted metabolomics of arginine-creatine metabolic pathway-related compounds in plasma: Application to identify potential biomarkers in pediatric chronic kidney disease, Anal. Bioanal. Chem. 408 (2016) 747−760.

[57] S. Mathialagan, A.D. Rodrigues, B. Feng, Evaluation of renal transporter inhibition using creatinine as a substrate in vitro to assess the clinical risk of elevated serum creatinine, J. Pharm. Sci. 106 (2017) 2535−2541.

[58] W.S. Waring, A. Moonie, Earlier recognition of nephrotoxicity using novel biomarkers of acute kidney injury, Clin. Toxicol. (Phila.) 49 (2011) 720−728.

[59] O. Lopes Abath Neto, L. Medne, S. Donkervoort, et al., MLIP causes recessive myopathy with rhabdomyolysis, myalgia and baseline elevated serum creatine kinase, Brain 144 (2021) 2722−2731.

[60] J.R. Poortmans, M. Francaux, Adverse effects of creatine supplementation: Fact or fiction? Sports Med. 30 (2000) 155−170.

[61] Z. Wang, B. He, C. Sun, et al., Study on tissue distribution of a variety of endogenous metabolites by air flow assisted ionization-ultra high resolution mass spectrometry imaging, Chin. J. Anal. Chem. 46 (2018) 406−411.

[62] J. Feng, X. Yang, R. Huang, et al., Development and validation of an LC-ESI-MS/MS method for the determination of nitidine chloride in rat plasma, J. Chromatogr. B Analyt. Technol. Biomed. Life Sci. 887-888 (2012) 43−47.